ACS Catalysis

Research Article

pubs.acs.org/acscatalysis

Structure Sensitivity Study of Waterborne Contaminant Hydrogenation Using Shape- and Size-Controlled Pd Nanoparticles

Danmeng Shuai,[†,§,■] Dorrell C. McCalman,[§,⊥] Jong Kwon Choe,[†,§] John R. Shapley,[‡,§] William F. Schneider,[§,⊥,∥] and Charles J. Werth*[,†,§]

[†]Department of Civil and Environmental Engineering, [‡]Department of Chemistry, and [§]Center of Advanced Materials for the Purification of Water with Systems, University of Illinois at Urbana−Champaign, Urbana, Illinois 61801, United States

[⊥]Department of Chemical and Biomolecular Engineering, [∥]Department of Chemistry and Biochemistry, University of Notre Dame, Notre Dame, Indiana 46556, United States

Supporting Information

ABSTRACT: Catalytic reduction with Pd has emerged as a promising technology to remove a suite of contaminants from drinking water, such as oxyanions, disinfection byproducts, and halogenated pollutants, but low activity is a major challenge for application. To address this challenge, we synthesized a set of shape- and size-controlled Pd nanoparticles and evaluated the activity of three probe contaminants (i.e., nitrite, *N*-nitrosodimethylamine (NDMA), and diatrizoate) as a function of facet type (e.g., (100), (110), (111)), ratios of low- to high-coordination sites, and ratios of surface sites to total Pd (i.e., dispersion). Reduction results for an initial contaminant concentration of 100 μM show that initial turnover frequency (TOF_0) for nitrite increases 4.7-fold with increasing percent of (100) surface Pd sites (from 0% to 95.3%), whereas the TOF_0 for NDMA and for diatrizoate increases 4.5- and 3.6-fold, respectively, with an increasing percent of terrace surface Pd sites (from 79.8% to 95.3%). Results for an initial nitrite concentration of 2 mM show that TOF_0 is the same for all shape- and size-controlled Pd nanoparticles. Trends for TOF_0 were supported by results showing that all catalysts but one were stable in shape and size up to 12 days; for the exception, iodide liberation in diatrizoate reduction appeared to be responsible for a shape change of 4 nm octahedral Pd nanoparticles. Density functional theory (DFT) simulations for the free energy change of hydrogen (H_2), nitrite, and nitric oxide (NO) adsorption and a two-site model based on the Langmuir−Hinshelwood mechanism suggest that competition of adsorbates for different Pd sites can explain the TOF_0 results. Our study shows for the first time that catalytic reduction activity for waterborne contaminant removal varies with the Pd shape and size, and it suggests that Pd catalysts can be tailored for optimal performance to treat a variety of contaminants for drinking water.

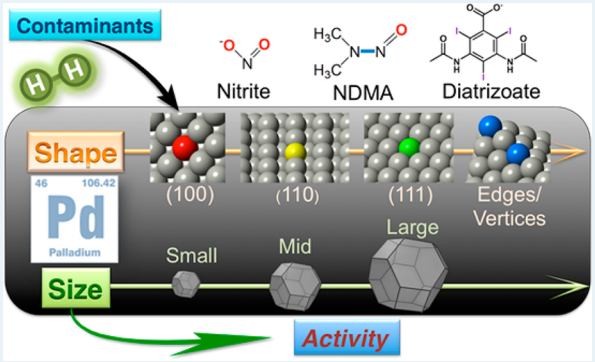

KEYWORDS: *shape control, structure-sensitive, palladium, hydrogenation, nitrite, N-nitrosodimethylamine, diatrizoate, contaminant*

INTRODUCTION

Pd-based catalytic hydrogenation has emerged as a promising technology to reduce a variety of priority contaminants in water,[1] including oxyanions (e.g., nitrate,[2,3] nitrite,[4] bromate,[5] chlorate,[6] perchlorate[7]), *N*-nitrosoamines (e.g., *N*-nitrosodimethylamine (NDMA)[8]), and halogenated compounds (e.g., trichloroethylene,[9] perchloroethylene,[10] polychlorinated biphenyls,[11] diatrizoate[12]). These contaminants come from various sources or processes (e.g., fertilizer,[13] rocket fuel,[14] X-ray contrast media,[15] degreasing,[16] dry cleaning,[16] and disinfection[17−19]). They are ubiquitously present in surface water,[14] groundwater,[14,20,21] or even treated water,[22−25] and they can adversely affect human health (e.g., carcinogenicity, mutagenicity, cytotoxicity, genotoxicity)[14,26−34] or ecological systems (e.g., result in eutrophication).[35,36] Compared with conventional water treatment technologies, such as ion-exchange, membrane processes, and biological treatment, catalytic hydrogenation is a promising technology because it uses readily available hydrogen gas as a clean reductant, it does not generate brine or a secondary waste stream,[37] it is robust to changes in water quality,[38,39] and it can simultaneously remove a suite of contaminants. Although catalytic treatment has been shown to be economically feasible for treating halogenated alkenes in groundwater,[38] reduction rates for other contaminants are often much slower (e.g., nitrate, NDMA, perchlorate).

Previous efforts to understand and improve catalytic activity have explored the effects of water quality parameters,[2,5,6]

Received: September 18, 2012
Revised: January 28, 2013
Published: January 30, 2013

Scheme 1. Nitrite, NDMA, and Diatrizoate Reaction Pathways on Pd[a]

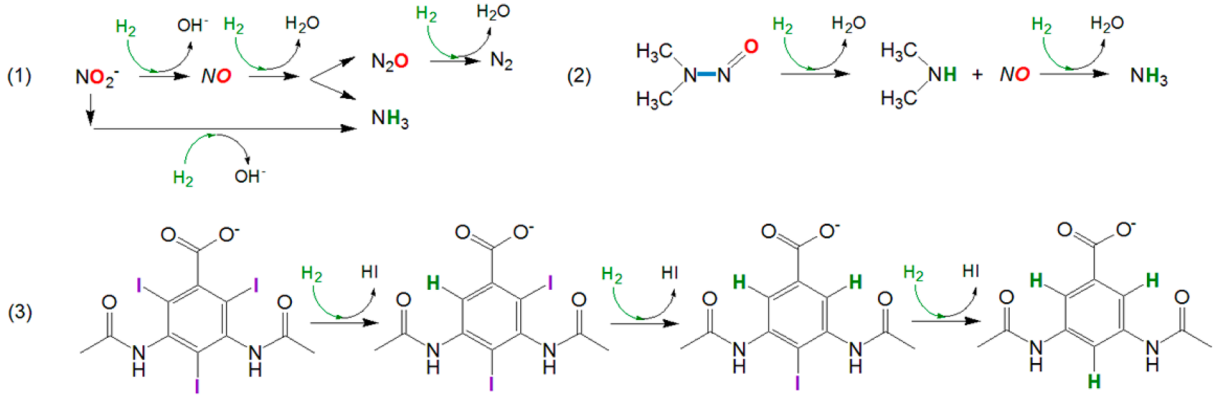

[a]Nitrite reduction is involved with sequential deoxygenation, and NO is a proposed intermediate (in italics) determining selectivity towards dinitrogen or ammonia.[3] Alternative reaction schemes for nitrite have been proposed,[57,58] but are not discussed because of the focus on nitrite reduction activity. NDMA reaction is initiated by N−N bond cleavage and then hydrogenation of NO as an intermediate (in italics) to ammonia exclusively.[8,53] Diatrizoate reduction proceeds through a stepwise hydrodeiodination to Dia-H_3.[12].

catalytic process control parameters,[3,40] and catalyst properties.[4,41−43] Of these, catalyst properties are the most difficult to evaluate because catalysts often contain an active metal (Pd in our case), typically loaded onto a support, and controlling either of these materials at the atomic scale has been a very challenging proposition. This is rapidly changing because advances in nanotechnology research are enabling unprecedented control of metal nanoparticle shapes and sizes as well as exploration of how these parameters enhance catalytic activity.

Shape-controlled metal nanoparticles have been prepared through liquid-based colloidal methods, using a variety of reactants and reaction conditions, to promote the formation of defined crystallographic orientations.[44−47] Nanoparticle growth is controlled either thermodynamically or kinetically at various rates, and a range of reductants, stabilizers, and etching agents are used to promote the formation of nanoparticles with desired shapes and sizes.[44] Metal nanoparticle size variations result in a change in the number of surface atoms and in the ratios of low-/high-coordination atoms (e.g., vertex, edge, and terrace).[48] Metal nanoparticle shape variations lead to a change in morphology and surface atom arrangement (e.g., cubes with only (100) terrace atoms; octahedra with only (111) terrace atoms; cuboctahedra with both (100) and (111) terrace atoms; and rods with all (100), (110), and (111) terrace atoms).[44] The effects of catalyst nanoparticle shape and size on activity have been studied for a series of structure-sensitive reactions, such as hydrogenation,[46,48,49] oxidation,[46] cross-coupling,[50] and electrochemistry.[51] However, no studies have explored the impacts of catalyst nanoparticle shape and size on reduction of waterborne contaminants.

The objective of our study is to explore for the first time catalytic structure sensitivity of Pd for hydrogenation of three probe contaminants in water. We prepared a series of different shape and size poly(vinyl-pyrrolidone) (PVP)-capped Pd nanoparticles (i.e., cubes, octahedra, cuboctahedra, and rods) to systematically vary the surface area of different facets, the ratio of the surface to bulk Pd atoms, and the ratio of low- to high-coordination surface Pd atoms. The three probe contaminants are nitrite, NDMA, and diatrizoate (Scheme 1); they are all environmentally relevant and difficult-to-treat water contaminants characterized by different reduction mechanisms. Nitrite is a direct intermediate in the reduction of nitrate, the most common groundwater contaminant in the United States.[20] It is converted in vivo to *N*-nitroso compounds, which are carcinogenic precursors.[52] NDMA is a neutral-charge organic compound unintentionally created during wastewater disinfection, and it is a carcinogen.[30] Diatrizoate is an acidic organic compound (pK_a = 3.4) used as an X-ray contrast agent. It has no known toxicological properties, but its recalcitrance to degradation may cause unanticipated health threats.[12] As shown in Scheme 1, nitrite reduction involves N−O bond cleavage (i.e., deoxygenation) and yields the end products dinitrogen and ammonia.[3] NDMA reduction proceeds through N−N bond cleavage and can yield the end products dimethylamine and ammonia.[8,53] Diatrizoate reduction requires C−I bond cleavage (i.e., dehalogenation) and yields a series of deiodinated intermediates, 3,5-diacetamidobenzoic acid (Dia-H_3), and iodide.[12] Reduced products of typical contaminants are generally less toxic compared with parent compounds,[54,55] but undesired byproducts (e.g., ammonia) still need to be controlled.[56]

We describe here the first experimental examination and computational analysis of Pd structure sensitivity in catalytic reduction of waterborne contaminants. We show that structure sensitivity depends on the contaminant type and concentration, that stability of the nanoparticle catalysts depends on constituents in the reaction solution, and that catalytic activity can be enhanced with proper Pd nanoparticle shape and size selection.

EXPERIMENTAL SECTION

Reagents. All chemicals were reagent grade and were purchased from Sigma-Aldrich [Na_2PdCl_4 ~ 99.995%, PVP M_W ~ 55 000, KBr ≥99.0%, ethylene glycol ≥99%, citric acid ≥99.5%, acetone ≥99%, methanol ≥99.9%, acetic acid ≥99.7%, sodium acetate ≥99.0%, acetonitrile ≥99.9%, triethylamine ≥99%, $Na_2HPO_4·2H_2O$ ~99%, NaH_2PO_4 ≥99.0%, NDMA, dimethylamine hydrochloride (DMA ~99%), 1,1-dimethylhydrazine (UDMH ~98%), sodium diatrizoate hydrate ≥99%, 3,5-diacetamidobenzoic acid (Dia-H_3), NH_4Cl ≥99%, KI ≥99.0%, 1-fluoro-2,4-dinitrobenzene (DNFB ≥99%), 4-nitrobenzaldehyde (NBA ~98%)], Fisher ($NaNO_2$ ≥99%, NaOH ≥98%), J. T. Baker (L-(+)-ascorbic acid ≥99.5%), or Cambridge Isotope Laboratories (^{15}N-$NaNO_2$ ≥98%, ^{15}N−N_2

dx.doi.org/10.1021/cs300616d | ACS Catal. 2013, 3, 453−463

≥98%, $^{15}N_2$−NDMA ≥98%). Tanks of H_2 (99.999%), NO (99.5%), and N_2O (99.999%) were purchased from Matheson Tri-Gas (Joliet, IL). All chemicals were used without further purification. All solutions were prepared in ultrapure water (18 MΩ cm), purified from deionized water in a Barnstead NANOpure System.

Synthesis and Characterization of Pd Nanoparticle Catalysts. Small and large Pd cubes, rods, cuboctahedra, and octahedra were each synthesized in one step on the basis of modifications of the protocols published by Xiong et al.[59,60] and Shao et al.[61] Briefly, Na_2PdCl_4 was the Pd precursor; PVP was used as a stabilizer; and ethylene glycol, ascorbic acid, or citric acid was used as the reductant. KBr was used to promote isotropic growth with (100) or (110) facets for cube or rod preparation because bromide preferentially chemisorbs on the (100) facet, alters the surface energies for different facets, and changes the thermodynamic favorability of facet growth.[59] The mixture of all reagents was stirred continuously while heating or refluxing at 80−130 °C for 3 h. Synthesized Pd nanoparticle catalysts were precipitated out of solution with acetone, collected with centrifugation, and washed with ultrapure water several times to remove excess PVP and other reactants. Finally, Pd nanoparticle catalysts were stored in aqueous stock suspensions. Duplicate batches of Pd cubes, cuboctahedra with small size, and octahedra with small and large sizes were prepared. Reproducibility of Pd nanoparticles with respect to shape, size, and catalytic performance was evaluated. The details of Pd nanoparticle catalyst synthesis are described in the Supporting Information (SI). To our knowledge, we are the first to report the one-step synthesis method for large-sized octahedra; in previous work, epitaxial growth on Pd seeds was reported.[48] Large-sized octahedra were synthesized with modified protocol for large-sized cuboctahedra,[60] and a slower mixing rate for Pd precursor and ethylene glycol was used (5 mL h^{-1} other than 45 mL h^{-1} for cuboctahedra). Slower mixing reduces the number of nuclei and facilitates the size growth of each nanoparticle. In addition, slower mixing also enhances complete shell formation for octahedra, whereas faster injection induces cuboctahedron production with truncated edges.

Transmission electron microscopy (TEM) with ImageJ was used to determine the shapes and sizes of the Pd nanoparticle catalysts. Geometric illustrations of Pd cubes, rods, cuboctahedra, and octahedra are shown in Figure 1. Edge lengths or diameters of Pd nanoparticles were measured, and dispersion (i.e., percentage of surface Pd atoms relative to total Pd atoms in bulk), surface fractions of each facet (e.g., surface fraction of (100) facet is the ratio of (100) surface Pd atoms to total Pd surface atoms), and surface fraction of terrace sites (i.e., surface fraction of high coordination sites, it is the ratio of terrace Pd atoms to total surface Pd atoms) were calculated for each nanoparticle on the basis of the measured geometry.[62] This approach has been widely used for calculating surface area and the number and percentage of specific surface sites (e.g., terrace, edge, corner),[63−65] and several spectroscopic and microscopic analyses have evaluated its applicability (e.g., CO chemisorption,[66] scanning tunneling microscopy[67]). The percent number purity, the ratio of the number of Pd nanoparticles with the desired shape to the total nanoparticle number, was also evaluated for each sample. About 300 Pd nanoparticles per sample were measured and evaluated for geometric properties and purity. The details of calculations are described in the SI.

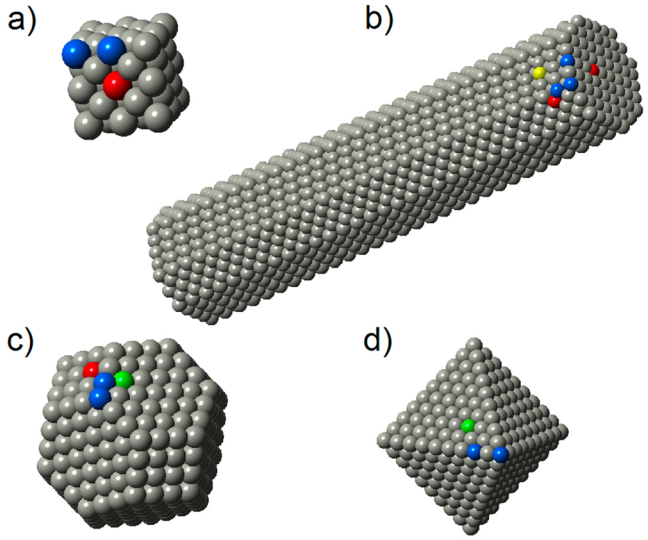

Figure 1. Geometric schematics of Pd cubes, rods, cuboctahedra, and octahedra. Blue, red, yellow, and green atoms represent edge/vertex, (100) site, (110) site, and (111) site, respectively.

X-ray powder diffraction (XRD) was used to characterize the size (in addition to characterization with TEM) and crystallinity of Pd nanoparticle catalysts. Full pattern refinement was performed in TOPAS (Bruker AXS, Inc., Version 3) using a Pd CIF file,[68] and the crystallite size was estimated on the basis of the integral breadth, assuming the intermediate crystallite size broadening modeled by a Voigt function.[69] X-ray photoelectron spectroscopy (XPS) was used to characterize impurities on the surfaces of Pd nanoparticle catalysts after extensive cleaning with acetone and ultrapure water to remove residual PVP, Cl^-, and Br^-. The binding energy scale was referenced to the aliphatic C 1s line at 285.0 eV. Pd catalyst loading for each catalytic run was calculated on the basis of the Pd content of a stock suspension, which was analyzed by inductively coupled plasma mass spectrometry (ICP-MS). Details of characterization methods are described in the SI.

Hydrogenation Reaction and Analytical Methods. Hydrogenation experiments were conducted in a 60 mL serum bottle equipped with a Teflon-coated magnetic stir bar and septum-sealed stoppers, all at 21 ± 1 °C. The bottles were filled with 20 or 40 mL of phosphate buffer (pH = 7, buffer concentration is 10 times the contaminant concentration), and amended with 0.2 mg of Pd catalysts (i.e., 10^{-2} or 5×10^{-3} g L^{-1} as catalyst loading). The suspension was sparged with H_2 for 30 min to remove oxygen in the suspension and headspace, to reduce oxidized catalyst surfaces, and to saturate the headspace and water with H_2. To initiate reaction, hydrogen presparged nitrite, NDMA, or diatrizoate stock solution was amended to the suspension at time zero while mixing at 560 rpm. A high and a low initial concentration of nitrite were evaluated. The high concentration was 2 mM; the low concentration was 100 μM and was chosen to match initial NDMA and diatrizoate concentrations and to explore structure sensitivity effects. The initial concentrations were chosen higher than environmental concentrations observed in drinking water to satisfy equipment detection limits and to facilitate accurate analysis. The molar ratio between contaminant and surface Pd atoms ranges from 3.2 to 8.4 for all three contaminants at 100 μM, whereas the molar ratio ranges from 128 to 334 for nitrite at 2 mM. The difference in molar ratios for a set contaminant

dx.doi.org/10.1021/cs300616d | ACS Catal. 2013, 3, 453−463

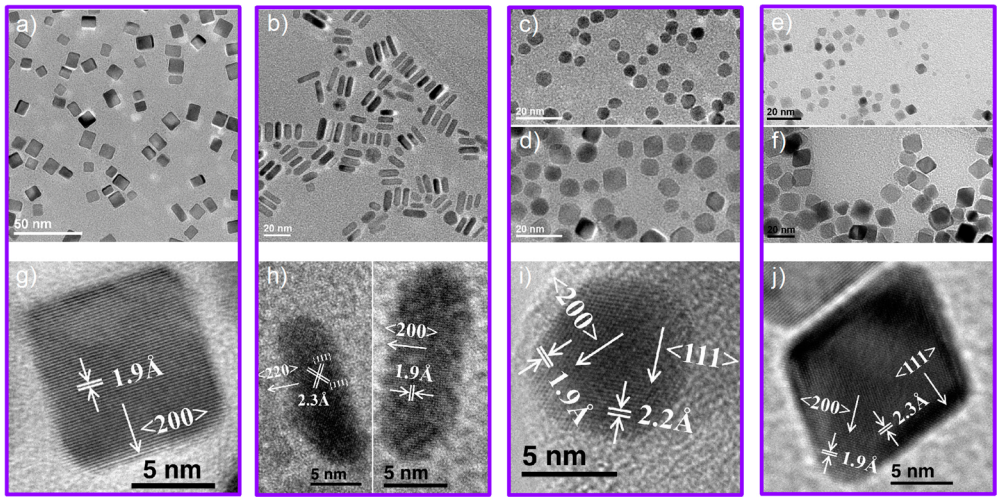

Figure 2. Low-magnification and high-resolution TEM images of Pd cubes (a, g), rods (b, h), cuboctahedra (c, d, and i), and octahedra (e, f, and j). Images c and d are cuboctahedra of small and large size, and e and f are octahedra of small and large size. Lattice spacing is indicated in high-resolution images. Enlarged images are shown in SI Figure S2.

concentration is due to variations in shape, size, and corresponding dispersion values for Pd nanoparticle catalysts. During reaction, 0.5 mL of sample was withdrawn by syringe at different time intervals, filtered through centrifugal filters (Amicon Ultra-0.5, Ultracel-30 Membrane, 30 kDa, Millipore), and stored in a refrigerator at 4 °C before analysis. Dilution by ultrapure water was necessary to analyze some samples. Control experiments were performed with various catalyst loadings and mixing rates; they indicated that H_2 was essential for reaction and was present in excess and that external mass transfer limitations were insignificant. Complete mass balances were observed in contaminant reductions. Details of the control experiments are described in the SI. All batch reactions were performed three to six times.

The nitrite and iodide anions were analyzed using ion chromatography (Dionex ICS-2000, Dionex IonPac AS18 and AS19 columns). NDMA, DMA, UDMH, diatrizoate, and Dia-H_3 were analyzed using high performance liquid chromatography (Shimadzu Prominence LC-20AT, Dionex Acclaim 120 C18 column). Ammonia was measured using the Hach salicylate method (low range, 0.02 to 2.50 mg L^{-1} NH_3–N, method 10023) and a Hach DR/4000U UV–vis spectrophotometer. Gas samples were analyzed using gas chromatography–mass spectroscopy (Varian 4000 GC/MS, CP-Molsieve 5 Å column) for ^{15}N-labeled NO, nitrous oxide, and dinitrogen.

Data Analysis. All contaminants follow pseudo-first-order kinetics for decay of at least 50% of the initial concentrations, and rate constants were obtained from linear regressions of the natural log of relative concentrations versus time plots. The initial turnover frequency (TOF_0, min^{-1}), the number of contaminant molecules reduced per site per minute, was calculated by dividing the product of the pseudo-first-order rate constant (k, min^{-1}) and the initial contaminant concentration (C_0, mol L^{-1}) by the concentration of surface Pd ($C_{surface\ Pd}$, mol L^{-1}), as shown in the following equation:

$$TOF_0 = \frac{kC_0}{C_{surface\ Pd}} = \frac{kC_0M}{C_{Pd}D} \quad (1)$$

$C_{surface\ Pd}$ is calculated by dividing the product of Pd catalyst loading (C_{Pd}, g L^{-1}) and dispersion (D) by Pd atomic weight (M, 106.4 g mol^{-1}). The kinetics are closely pseudo-first-order in nitrite up to one-half-life, and thus, TOF_0 is representative of the intrinsic rate over that period of time.

DFT Calculations of Hydrogen, Nitrite, and NO Adsorption. To provide some insights into the observed structure sensitivity in the nitrite reduction, periodic supercell density functional theory was used to compare the binding energies and configurations of H_2, nitrite, and NO on the (100), (110), (111), and (211) facets of Pd. All slabs were four layers thick. The atoms in the bottommost layer were fixed at their bulk positions while all other atoms, including adsorbates, were allowed to relax. The energy of the slabs was converged to within 0.005 eV with respect to increased k-point density. The generalized gradient approximation of Perdew and Wang[70] was used to treat electron exchange and correlation. Core electrons were treated with the projector augmented wave method of Blöchl.[71] All calculations were done using the Vienna ab initio Simulation Package (VASP).[72,73] The plane wave basis set included waves up to an energy cutoff of 400 eV, and forces were converged to 0.05 eV $Å^{-1}$. The built-in dipole corrections of VASP were used to ensure accurate calculation of the nitrite gas phase energy. With these corrections, the calculated electron affinity was within 0.1 eV of the experimental value.

Adsorption free energies of neutral adsorbates are straightforward to compute. To compute the free energy change of aqueous nitrite adsorption, we assume that adsorption is coupled to the hydrogen dissociation half-reaction to conserve charge,

$$NO_2^-(aq) + H^+(aq) + * \rightarrow NO_2* + \frac{1}{2}H_2(g) \quad (2)$$

where the asterisk (*) denotes a surface site. We take advantage of known experimental thermochemical data and the fixed experimental H_2 pressure and pH. The approach follows the method popularized by Nørskov and co-workers[74] and used to model the electrochemistry of many ions, including borohydride, acetate, phosphate, and sulfate.[75–77] The computational details are included in the SI.

EXPERIMENTAL RESULTS

Synthesis and Characterization of Pd Nanoparticle Catalysts with Controlled Shapes and Sizes. Low-

dx.doi.org/10.1021/cs300616d | ACS Catal. 2013, 3, 453–463

magnification and high-resolution TEM images of Pd cubes, rods, cuboctahedra, and octahedra are shown in Figure 2. Low-magnification TEM images were used to characterize Pd nanoparticle shapes and sizes and to calculate percent number purities. Pd cubes were prepared with >95.5% purity, and their edge lengths were 9.3 ± 2.1 and 8.7 ± 1.8 nm for duplicate batches. Pd rods were prepared with >92.2% purity, and their longitudinal and transversal lengths were 13.2 ± 2.4 and 4.3 ± 0.8 nm, corresponding to an aspect ratio of 3.0. Both small and large cuboctahedra had almost 100% purity, and their effective diameters were 5.3 ± 1.1 and 5.7 ± 1.0 nm for duplicate batches and 8.6 ± 1.9 nm, respectively. Both small and large octahedra were prepared with >85.1% purity, and their edge lengths were 4.5 ± 0.7 and 4.3 ± 0.6 nm and 10.7 ± 1.4 and 10.5 ± 1.2 nm for duplicate batches, respectively.

High-resolution TEM was used to characterize Pd nanoparticle lattice spacing and to confirm their monocrystallinity and crystallographic plane boundaries. Pd nanoparticle crystallinity and size were also characterized by XRD. A representative diffractogram is shown in SI Figure S3a. All Pd samples share similar diffractograms, which confirm their crystalline rather than amorphous structures. Pd nanoparticle diameters from XRD were 8.9 and 8.7 nm for duplicate batches of prepared cubes, 5.8 nm for rods, 4.9 and 4.5 nm for duplicate batches of small cuboctahedra, 8.8 nm for duplicate batches of large cuboctahedra, 3.9 and 4.3 nm for duplicate batches of small octahedra, and 10.5 and 10.5 nm for duplicate batches of large octahedra. For all samples but rods, the XRD values agree adequately with those measured by TEM. Unlike other shapes, rods were prepared with isotropic growth toward one direction; hence, their size characterized by XRD represents some average of longitudinal and transverse dimensions. To compare rod size characterized by TEM and XRD, we calculated the edge length for hypothetical cubes having the same volume as rods, and the calculated value of 5.9 nm is close to XRD size determination of 5.8 nm.

After extensive cleaning of synthesized nanoparticles by acetone and ultrapure water, XPS was used to determine if residual chemicals used during synthesis remained on Pd surfaces. Representative XPS spectra are shown in SI Figure S3b–d; all other Pd samples exhibit similar spectra. Only O, N, C, and Pd were detected; neither Br nor Cl was observed, even with high-resolution XPS analysis. N is used as an indicator to estimate residual stabilizer PVP on the Pd surface, and it agrees with a previous study using similar synthesis protocols and cleaning procedures.[48] Different stabilizers can modify the surface properties and impact catalytic behavior;[78−80] therefore, we used the same PVP stabilizer to minimize interference. In addition, quantitative analysis of the N-to-surface Pd ratio yields 6.3 ± 3.4 (i.e., the PVP monomer to bulk Pd ratio is 1.4 ± 1.0), suggesting that the residual amount of PVP is similar across all samples. Absolute amounts of residual PVP were calculated from the N-to-surface Pd ratios, Pd nanoparticle dispersions, and ICP-MS analyses of the Pd content, indicating that more than 90% of PVP was removed from each of the prepared catalysts. Previous studies of 1,3-cyclooctadiene hydrogenation[81] and Suzuki coupling[64] suggest that residual PVP at this loading will not affect reaction kinetics, but comparisons of reaction kinetics on low PVP versus PVP free catalyst surfaces were not performed.

A recent study used UV-ozone oxidization to effectively eliminate residual PVP on supported cubic Pd nanoparticles without altering their shapes and sizes, and the TOF for acetylene hydrogenation increased by 4 fold, which indicates residual PVP partially blocked reactive Pd sites and reduced activity.[82] However, PVP-eliminated Pd nanoparticles are not stable and tend to aggregate in aqueous solution and, thus, cannot be used in our system. It is possible that residual PVP influences catalytic activity in our study by hindering access of reactants to active sites. However, our results suggest that the presence of residual PVP does not mask the influence on activity of different Pd sites. Further work is required to elucidate any effects residual PVP might have on intrinsic Pd nanoparticle activity.

Pd Nanoparticle Catalysts for Nitrite Reduction. Nitrite reduction activity was evaluated for all Pd nanoparticle catalysts. Figure 3 shows measured TOF_0 as a function of the fraction of

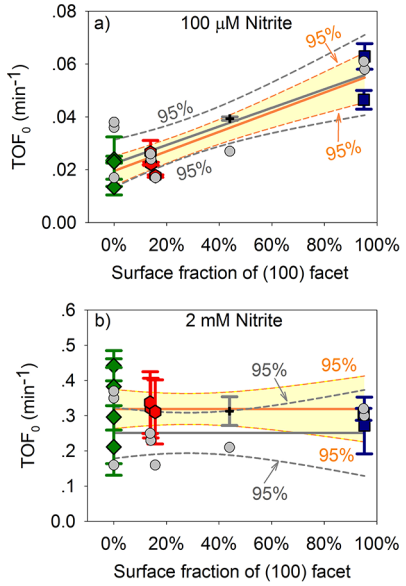

Figure 3. Initial turnover frequency (TOF_0) for nitrite reduction versus surface fraction of (100) facet of Pd nanoparticle catalysts. The initial nitrite concentration was (a) 100 μM and (b) 2 mM, respectively. Green diamond, red hexagon, gray cross, and blue cube represent experimental data from octahedral, cubocatahedral, rod, and cubic Pd nanoparticle catalysts. Surface fraction of the (100) facet of Pd nanoparticle catalysts is the number of (100) atoms to the number of surface Pd atoms. Error bars represent standard deviations of replicates. Orange solid lines are linear regressions of experimental TOF_0 versus surface fraction of (100) facet, and orange dashed lines and enclosed light yellow region represent the 95% confidence interval bands of linear regressions of experimental data. Gray circles represent model simulation results, gray solid lines are linear regression of model estimated TOF_0 versus surface fraction of (100) facet, and gray dashed lines represent the 95% confidence intervals of linear regressions of model data.

(100) surface facets at 100 μM and 2 mM initial nitrite concentrations. At the higher initial concentration, TOF_0 is the same within experimental uncertainty, evidencing no structure sensitivity. Significantly, at the lower initial nitrite concentration, the nitrite reduction TOF_0 increases in proportion to the surface fraction of (100) facets. We applied linear regression fits to both sets of data. The fit to the high concentration data has a slope of 0, and the low concentration data are fit by a positively sloping line with R^2 = 0.86. The 95% confidence intervals of regression also support a positive correlation between (100) facet and TOF_0. Linear regressions between TOF_0 and surface fractions of other facets, dispersion, and

dx.doi.org/10.1021/cs300616d | ACS Catal. 2013, 3, 453−463

surface fraction of terrace sites were also explored, but R^2 values were less than 0.25 in all cases.

The (100) facets of Pd nanoparticles are reported to be more active for the oxygen reduction reaction (ORR) than the other terrace facets, such as (111). This difference has been attributed to a lower coverage of surface-adsorbed OH on the (100) sites and, consequently, more sites available for reaction.[61] In contrast, the nitrite reduction TOF_0 is not statistically different on different crystal faces at a high initial nitrite concentration (2 mM). Because the surface fraction of a specific facet is dependent on the Pd nanoparticle shape (SI Figure S4d–f), we conclude that the TOF_0 for nitrite reduction is shape-dependent at low initial nitrite concentration but independent of both shape and size at high initial nitrite concentration. This is the first report that the dependence of reaction activity on nanoparticle catalyst shape and size can vary with reactant concentration. DFT and mathematical model simulations will be used to interpret the structure sensitivity of nitrite reduction in a later section.

Pd Nanoparticle Catalysts for NDMA and Diatrizoate Reduction. NDMA and diatrizoate reduction TOF_0 on Pd nanoparticle catalysts with different shapes and sizes are shown in Figure 4. TOF_0 for both contaminants increase linearly with

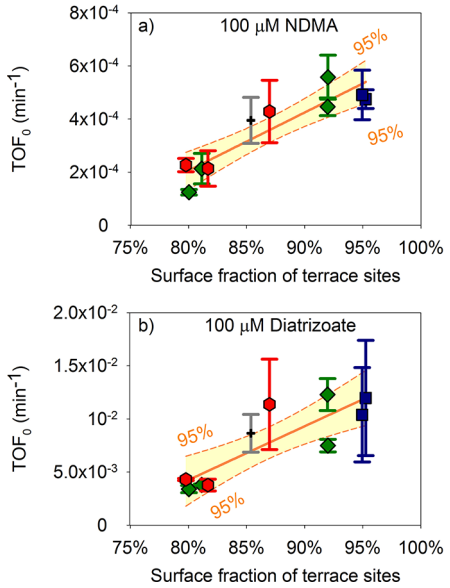

Figure 4. Initial turnover frequencies (TOF_0) for (a) NDMA and (b) diatrizoate reduction versus surface fraction of terrace sites of Pd nanoparticle catalysts. Initial concentrations were 100 μM. Green diamond, red hexagon, gray cross, and blue cube represent data from octahedral, cubocatahedral, rod, and cubic Pd nanoparticle catalysts. Surface fraction of terrace sites of Pd nanoparticle catalysts is the number of terrace atoms to the number of surface atoms. Error bars represent standard deviations of replicates. Orange solid lines are linear regressions of TOF_0 versus surface fraction of terrace sites, and orange dashed lines and enclosed light yellow region represent the 95% confidence intervals of linear regressions.

increasing surface fraction of terrace sites (e.g., surface faction of the sum of (100), (111), and (110) sites, with 95% confidence intervals), and R^2 = 0.69 and 0.73 for NDMA and diatrizoate, respectively. Linear regressions between TOF_0 and both surface fractions of individual facets and dispersion were also explored, but R^2 values were <0.27 in these cases. Hence, NDMA and diatrizoate reduction activity is only size-dependent, because the surface fraction of terrace sites relies on Pd nanoparticle size for all shapes (SI Figure S4c). Each NDMA molecule was proposed to bind to three neighboring Pd atoms during reduction,[83] and diatrizoate may also bind to multiple Pd sites because of its large molecular size and abundant moieties and functional groups, such as the carboxylic acid group, benzene ring, iodine, and amide group. Benzene hydrogenation was studied on Pt (111) and Pd (111) by density functional theory simulations, and benzene and its hydrogenation intermediates anchor on catalyst surfaces through multiple sites.[84] Large Pd nanoparticles with relatively more terrace sites (SI Figure S4c) provide strong and stable multisite binding to NDMA, diatrizoate, and their reduction intermediates, in contrast to edge and vertex sites; therefore, faster reduction kinetics were observed.

Shape and Size Stability of Pd Nanoparticle Catalysts. The shape and size stability of Pd nanoparticle catalysts is a concern for the validity of the aforementioned data. Pd nanoparticle catalysts may change their shape and size during a reaction, especially the dissolution of low-coordination atoms at edge and corner sites by Ostwald ripening,[50] by interaction with chemicals present in the reaction mixture,[85] or by aggregation.[86,87] Catalytic performance can also vary with catalyst shape and size.[50] By TEM characterization after reaction, Pd nanoparticle catalysts did not change shape or size during reaction with nitrite or NDMA over a period of 4 h to 5 days (SI Figure S5). The same is true during reaction with diatrizoate, even up to 12 days, except for reaction with small octahedra (SI Figure S5). Small octahedra ~4 nm in size changed shape to spherelike particles (SI Figure S5). During diatrizoate reduction, I^- is liberated; it has been shown to strongly chemisorb to Pd.[88] I^- changes Pd nanoparticle shape either by atomic rearranging or by etching. To test this possibility, we exposed a sample of small octahedra Pd nanoparticles to 35 μM I^-, I^- and nitrite, or I^- and NDMA for 9 h; this is the same concentration of I^- released during diatrizoate reduction. Results show that the sample with only I^- changed shape to near-sphere (SI Figure S6). No shape-change was observed when the octahedra Pd nanoparticles were exposed to mixtures of I^- and nitrite or to I^- and NDMA (SI Figure S6). These results suggest that I^- and nitrite or NDMA compete for adsorption sites on the Pd surface and that nanoparticle shape may be maintained by amending inert species with sufficient concentration.

MODEL RESULTS AND DISCUSSION

DFT Calculation and Two-Site Model Simulation for Structure-Sensitive Nitrite Reduction. Several factors could cause the apparent nitrite reaction activity dependence on nanoparticle catalyst shape and size to change with concentration. These include pH, residual organic molecules on the Pd surface, and intrinsic reactivity/adsorption on different Pd facets. Reaction solutions were well buffered during reaction (pH = 7.5 ± 0.2), and there was no observed difference or change in pH between high and low concentrations of nitrite. The majority of PVP stabilizer had been removed during extensive catalyst cleaning procedures, and the amounts remaining were relatively uniform, so this was estimated not to inhibit catalyst reduction kinetics (discussed in the SI).

We hypothesize that variations in intrinsic reactivity and adsorption on the different Pd facets are responsible for the difference in structure sensitivity at low and high nitrite

dx.doi.org/10.1021/cs300616d | ACS Catal. 2013, 3, 453–463

concentrations. To evaluate our hypothesis, we used DFT to calculate the adsorption free energies of H_2, nitrite, and NO on different Pd facets. Furthermore, we developed a two-site mathematical model based on a Langmuir−Hinshelwood mechanism that is consistent with both our experimentally measured data and our DFT calculations.

We identified the lowest energy binding configurations of nitrite on the Pd (100), (110), (111), and (211) sites as calculated by DFT;the results are shown in Figure 5. On these

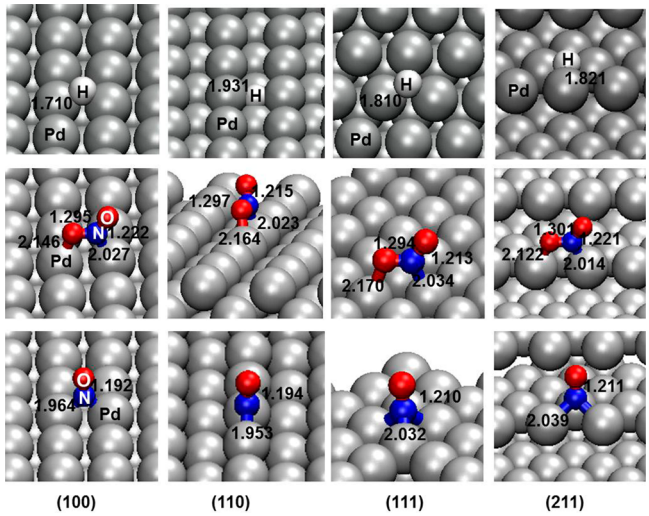

Figure 5. Most stable binding configurations of H (top panel), nitrite (middle panel), and NO (bottom panel) on Pd (100), (110), (111), and (211). Bond lengths are shown in angstroms. Pd atoms are gray, nitrogen atoms are blue, oxygen atoms are red, and hydrogen atoms are white.

facets, nitrite prefers to bind by forming two bonds with the surface atoms: a Pd−N bond and a Pd−O bond. The configuration with two Pd−O bonds was the next favorable. Hydrogen atoms bind most favorably in bridge sites on Pd (100) and (110) and in 3-fold sites on Pd (111) and (211). NO binds in bridge sites on (100) and (110) and in 3-fold hollow sites on (111) and (211). The free energy change upon adsorption of aqueous H_2, aqueous nitrite, and aqueous NO are shown in Table 1. The relevant equations are eqs 2 and the following equations, 3 and 4.

$$\frac{1}{2}H_2(aq) + * \rightarrow H* \tag{3}$$

$$NO(aq) + * \rightarrow NO* \tag{4}$$

The numbers reported correspond to a pH of 7.5; hydrogen, nitrite, and NO activities of 1; and a H_2 partial pressure of 1 atm. It can be seen that the (100) facet forms stronger bonds with the adsorbates because adsorption free energy changes associated with that surface are the most negative or the least positive, that is, the most exergonic. It can also be seen that the free energy of adsorption of NO, which ranges from −2.21 to −1.90 eV, is far more negative than the free energy of adsorption of nitrite (0.13−0.89 eV) and H_2 (−0.7 to −0.26 eV). This indicates that NO adsorption is far more exergonic than either nitrite or H_2 adsorption.

These results highlight the different behavior of the (100) facet as well as the likely important role of adsorbed NO as a surface intermediate. Motivated by this observation and the

Table 1. DFT-Computed Adsorption Free Energies vs Pd Facet

species	Pd facet	ΔG^0_{ads} (eV)[a]
H_2	(100)	−0.70
	(110)	−0.26
	(111)	−0.39
	(211)	−0.36
nitrite	(100)	0.13
	(110)	0.42
	(111)	0.89
	(211)	0.41
NO	(100)	−2.21
	(110)	−1.90
	(111)	−1.90
	(211)	−1.98

[a]The free energy change of adsorption is calculated as zero-point corrected gas phase binding energies plus entropy, solvation, pH, and temperature corrections. The experimental temperature is 294.15 K (i.e., 21 °C), and the pH is 7.5. The standard state conditions for pressure and activity were taken to be 1 atm and 1, respectively.

observed correlation of TOF_0 with the (100) facet fraction, we constructed a two-site kinetic model in which (100) sites and non-(100) sites are designated as sites 1 and sites 2, respectively. We take nitrite and H_2 as the initial reactants and NO as a likely surface intermediate. Dinitrogen, ammonia, and nitrous oxide bind much more weakly to Pd than NO does,[89−92] so their accumulation on Pd surface sites is ignored. For sites 1, we included the following reactions in our model in addition to species adsorption shown in eqs 2−4:

$$NO_2*_1 + H*_1 \rightarrow NO*_1 + \text{other intermediates or products} \tag{5}$$

$$NO*_1 + H*_1 \rightarrow \text{other intermediates or products} \tag{6}$$

We assume the aqueous concentrations of H_2, nitrite, and NO are at equilibrium with surface concentrations, and adsorption constants are written as

$$K_{H_2,*_1} = \frac{[*_1 - H]^2}{[*_1]^2[H_2]} \tag{7}$$

$$K_{NO_2^-,*_1} = \frac{[*_1 - NO_2^-]}{[*_1][NO_2^-]} \tag{8}$$

$$K_{NO,*_1} = \frac{[*_1 - NO]}{[*_1][NO]} \tag{9}$$

in which $K_{X,*_1}$ is equilibrium adsorption constants for X at sites 1 (X = H_2, NO_2^-, or NO) (L mol^{-1}), $[*_1 - X]$ is surface concentration of X at sites 1 (mol L^{-1}), [X] is aqueous concentration of X (mol L^{-1}), and $[*_1]$ is the concentration of empty sites 1 (mol L^{-1}). H_2 is always in great excess compared with nitrite (shown in the SI), and we assume that the aqueous H_2 concentration reaches its solubility limit of 7.9×10^{-4} mol L^{-1} at 21 °C and 1 atm[93] and that it is constant during reaction.

Performing a site balance for sites 1, we have the following expression:

$$[*_1]_0 = [*_1] + [*_1 - H] + [*_1 - NO_2^-] + [*_1 - NO] \tag{10}$$

in which $[*_1]_0$ is the total concentration of sites 1 (mol L^{-1}).

dx.doi.org/10.1021/cs300616d | ACS Catal. 2013, 3, 453−463

Nitrite reduction rate ($r_{NO_2^-,*_1}$, mol L^{-1} min^{-1}) at sites 1 can be expressed as

$$r_{NO_2^-,*_1} = k_{NO_2^-,*_1}[*_1 - H][*_1 - NO_2^-] = k_{NO_2^-,*_1} \times \frac{([*_1]_0)^2\sqrt{K_{H_2,*_1}[H_2]}\,K_{NO_2^-,*_1}[NO_2^-]}{(1 + \sqrt{K_{H_2,*_1}[H_2]} + K_{NO_2^-,*_1}[NO_2^-] + K_{NO,*_1}[NO])^2} \quad (11)$$

in which $k_{NO_2^-,*_1}$ is the second-order rate constant (L mol^{-1} min^{-1}) for nitrite reduction at sites 1. Similarly, nitrite reduction rate at sites 2 ($r_{NO_2^-,*_2}$, mol L^{-1} min^{-1}), and NO reduction rate at sites 1 ($r_{NO,*_1}$, mol L^{-1} min^{-1}) and sites 2 ($r_{NO,*_2}$, mol L^{-1} min^{-1}), can be expressed as

$$r_{NO_2^-,*_2} = k_{NO_2^-,*_2} \times \frac{([*_2]_0)^2\sqrt{K_{H_2,*_2}[H_2]}\,K_{NO_2^-,*_2}[NO_2^-]}{(1 + \sqrt{K_{H_2,*_2}[H_2]} + K_{NO_2^-,*_2}[NO_2^-] + K_{NO,*_2}[NO])^2} \quad (12)$$

$$r_{NO,*_1} = k_{NO,*_1} \times \frac{([*_1]_0)^2\sqrt{K_{H_2,*_1}[H_2]}\,K_{NO,*_1}[NO]}{(1 + \sqrt{K_{H_2,*_1}[H_2]} + K_{NO_2^-,*_1}[NO_2^-] + K_{NO,*_1}[NO])^2} \quad (13)$$

$$r_{NO,*_2} = k_{NO,*_2} \times \frac{([*_2]_0)^2\sqrt{K_{H_2,*_2}[H_2]}\,K_{NO,*_2}[NO]}{(1 + \sqrt{K_{H_2,*_2}[H_2]} + K_{NO_2^-,*_2}[NO_2^-] + K_{NO,*_2}[NO])^2} \quad (14)$$

in which $k_{NO_2^-,*_2}$, $k_{NO,*_1}$, and $k_{NO,*_2}$ are rate constants (L mol^{-1} min^{-1}), $[*_2]_0$ is the total concentration of sites 2 (mol L^{-1}), and $K_{X,*_2}$ is equilibrium adsorption constants for X at sites 2 (X = H_2, NO_2^-, or NO) (L mol^{-1}). Site concentration is the number of specific sites per volume of reaction solution and it is calculated by

$$[*_1]_0 = \frac{F_1 mD}{MV} \quad (15)$$

$$[*_2]_0 = \frac{(1 - F_1)mD}{MV} \quad (16)$$

in which F_1 is the surface fraction of sites 1, m is the Pd weight for each reaction (g), D is dispersion of Pd nanoparticle catalysts, M is the atomic weight of Pd (106.4 g mol^{-1}), and V is the volume of reaction solution (L). Finally, the concentration variations of nitrite and NO with time are expressed as

$$\frac{d[NO_2^-]}{dt} = -r_{NO_2^-,*_1} - r_{NO_2^-,*_2} \quad (17)$$

$$\frac{d[NO]}{dt} = r_{NO_2^-,*_1} + r_{NO_2^-,*_2} - r_{NO,*_1} - r_{NO,*_2} \quad (18)$$

We solve the differential equations with initial inputs of reaction rate constants, equilibrium adsorption constants, and nitrite concentrations; obtain degradation of nitrite concentration time course profiles; and then calculate pseudo-first-order rate constants and TOF_0's according to the same methods used in Data Analysis. The model TOF_0 also represents the intrinsic rate from time zero to one-half-life of nitrite, like the experimental TOF_0. The differences between the experimental TOF_0 and model TOF_0 are minimized by the GlobalSearch algorithm in Matlab (version R2012a, Mathworks). GlobalSearch uses a scatter-search mechanism for generating start points and then uses a local solver to find the minimum of a constrained nonlinear multivariable function (fmincon) and by iteration searches for a single global minimum. The details of the optimized parameter values are shown in Table 2, and the model estimated TOF_0 values are plotted in Figure 3 (also listed in SI Table S1). Despite the fact that the DFT results were not used in seeding the optimization, best-fit results are consistent with the trends identified from the DFT calculations; that is, adsorption is more favorable on sites 1 than sites 2, and adsorption of NO is stronger than for nitrite and H_2. This correspondence gives confidence that the fitted parameter set is characteristic of the underlying kinetics. Linear regression of the model estimated TOF_0 was performed against surface fraction of (100) facets, and model results are compared with experimental results in Figure 3.

Table 2. Calculated Reaction Rate Constants and Equilibrium Adsorption Constants for H_2, Nitrite, and NO on Sites 1 and 2

Kinetics			
reduction rate constant (L mol^{-1} min^{-1})		values	k^1/k^2 [a]
nitrite	sites 1 ($k_{NO_2^-,*_1}$)	5.38×10^8	8.97×10^{-1}
	sites 2 ($k_{NO_2^-,*_2}$)	6.00×10^8	
NO	sites 1 ($k_{NO,*_1}$)	3.08×10^6	4.85×10^{-2}
	sites 2 ($k_{NO,*_2}$)	6.36×10^7	
Adsorption			
equilibrium adsorption constant (L mol^{-1})		values	K^1/K^2 [a]
H_2	sites 1 ($K_{H_2,*_1}$)	6.06	4.25
	sites 2 ($K_{H_2,*_2}$)	1.43	
nitrite	sites 1 ($K_{NO_2^-,*_1}$)	1.70	2.68
	sites 2 ($K_{NO_2^-,*_2}$)	0.64	
NO	sites 1 ($K_{NO,*_1}$)	1.94×10^5	14.2
	sites 2 ($K_{NO,*_2}$)	1.36×10^4	

[a] The ratio between values at sites 1 and those at sites 2.

The fitted reduction rate constants for nitrite are 8.47−194 times greater than those for NO, suggesting that NO reduction is the rate-limiting step and NO will accumulate on the catalyst surfaces. This trend agrees well with previous experimental results from our group that the pseudo-first-order rate constant for NO reduction on a Pd−In catalyst is 15.5-fold less than that of nitrite.[58] From the model fits, nitrite reduction is 174 times faster than NO reduction on site 1, but is only 9.44 times faster on site 2, consistent with greater NO accumulation on sites 1 than on sites 2. The calculated equilibrium adsorption constants for NO are 2.24×10^3 to 1.36×10^5 times greater than those for H_2 and are 7.97×10^3 to 3.04×10^5 times greater than those for nitrite, suggesting that NO binds significantly more strongly on the Pd surface than does H or nitrite. Equilibrium adsorption constants for H_2, nitrite, and

dx.doi.org/10.1021/cs300616d | ACS Catal. 2013, 3, 453−463

NO on sites 1 are 4.25, 2.68, and 14.2 times greater than those on sites 2.

These comparisons are in excellent qualitative correspondence with the DFT computational results, which predict that the NO adsorption free energy is more negative than that for H_2 or nitrite and that adsorption free energies are more negative on the (100) facet. In fact, the DFT results imply much larger facet dependence on the adsorption free energies than that observed, likely reflecting the neglect of coverage effects on binding energies of all species. For example, DFT calculations show that the absolute NO adsorption energy decreases from −2.21 eV reported here on a dilute (111) surface to −1.31 eV at 3/4 monolayer coverage. Finally, the experimental and model TOF_0's are not statistically different from each other, as indicated by the overlap in the 95% confidence interval linear regression bands. Hence, the model TOF_0 matches adequately with the experimental TOF_0. Results clearly indicate that both intrinsic activity and adsorption of H_2, nitrite, and NO influence the structure sensitivity of nitrite reduction.

On the basis of DFT simulations and the two-site mathematical model, we can envision how dependence of the TOF_0 on the catalyst shape and size varies with the initial nitrite concentration. A conceptual model is illustrated in Scheme 2.

Scheme 2. Conceptual Two-Site Model for Scenarios (a) Low Initial Nitrite Concentration and (b) High Initial Nitrite Concentration[a]

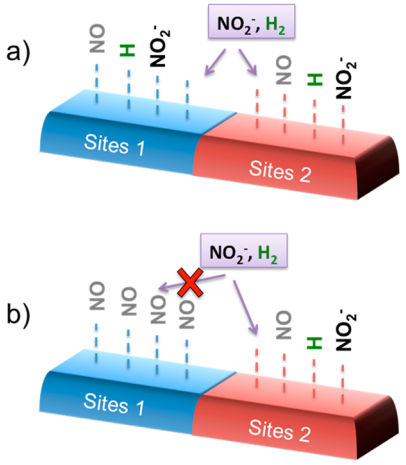

[a]H_2 and nitrite adsorb on either sites 1 or 2, and they react to produce NO on surface Pd sites. Sufficient available sites are present for H_2 and nitrite adsorption/reaction at low initial concentration, but NO accumulates on sites 1 at high initial concentration, and hence, it shifts nitrite reduction to sites 2.

Reactant H_2 and nitrite adsorb on surface Pd sites 1 or 2, react, and form NO (or a closely related intermediate, e.g., NOH) at the beginning stage of reduction. At low initial nitrite concentration, there are plenty of available surface Pd sites for H_2, nitrite, NO adsorption and reaction, and no significant adsorption competition among H_2, nitrite, and NO is observed. We note that the specific nitrite reduction rate constant on sites 1 is slightly smaller than that on sites 2 (10.3% smaller, Table 2), but the overall reduction rate is still faster for sites 1 because both H_2 and nitrite bind more strongly (4.25 and 2.68 times strongly, Table 2). The nitrite reduction rate is proportional to the product of the site specific reduction rate constant, the square root of the equilibrium adsorption constant of H_2, and the site-specific equilibrium adsorption constant of nitrite (eqs 11 and 12, denominators are 1 because of very low coverage), so the overall reduction rate on sites 1 is 4.95 times faster than on sites 2. Hence, catalysts with more sites 1 have a higher TOF_0 for nitrite reduction. At high initial nitrite concentration, fast nitrite reduction and slow NO reduction results in the accumulation of NO on sites 1 at the initial stage of reaction, and it blocks the further adsorption/reaction of H_2 and nitrite on sites 1 and shifts nitrite reduction to sites 2. The adsorption competition among H_2, nitrite, and NO compromises the fast nitrite reduction on sites 1, and hence, a nonselective overall reduction rate is observed.

To further support the proposed conceptual model, we estimated the change of the relative rate on sites 1 and 2 with an initial nitrite concentration on the basis of the mathematical two-site model and best-fitted parameter values. We calculated the average TOF from time zero to half-decay of the initial nitrite concentration for both sites (TOF_{50}, SI Table S2) by dividing the integral of nitrite reduction rate ($r_{NO_2^-}$, mol L^{-1} min^{-1}) over time by the product of the concentration of the surface Pd ($C_{surface\ Pd}$, mol L^{-1}) and half-time (T_{50}, min). It is expressed as

$$TOF_{50} = \frac{\int_0^{T_{50}} r_{NO_2^-}\, dt}{C_{surface\ Pd} T_{50}} \quad (19)$$

We also calculated the turnover number (TON) at the end of reduction for both sites (SI Table S3). The TON is the number of nitrites converted per site, and it is the integral of the TOF with respect to time. The TOF or TON ratio (R) between sites 1 and 2 was calculated for each catalyst under both low and high nitrite reduction, and it is expressed as

$$R = \frac{TOF_{50}\ (\text{or TON})\ \text{at sites 1}}{TOF_{50}\ (\text{or TON})\ \text{at sites 2}} \quad (20)$$

R is 1.2−1.8 times greater at 100 μM nitrite reduction (i.e., R(100 μM)) than that at 2 mM nitrite reduction (i.e., R(2 mM)) for the same catalyst, which indicates that the relative activity of sites 1 to sites 2 is inhibited with high nitrite concentration. The variation of the ratios with initial nitrite concentration supports our conceptual model (Scheme 2), which predicts the competition scenarios among H_2, nitrite, and NO and reaction shift from sites 1 to site 2 at high nitrite concentration. In addition, we evaluated nitrite and NO solution concentration profiles, also according to the mathematical model. Only negligible NO is formed in solution during reduction for all catalysts because of the much greater affinity of NO to the Pd surface compared with that of nitrite; one representative concentration profile is shown in SI Figure S7. This agrees with our experimental observations because no NO was detected. Experimental data, DFT simulations, and the two-site mathematical model support each other, and they provide insights toward explaining catalytic activity shape-dependence change with nitrite concentration.

CONCLUSIONS

Catalytic reduction with Pd has emerged as a promising technology to remove a suite of persistent contaminants from drinking water, including oxyanions, disinfection byproducts, and halogenated pollutants, but less than optimum activity for many contaminants affects its prospects for application.[1] To

dx.doi.org/10.1021/cs300616d | ACS Catal. 2013, 3, 453−463

address these challenges, we synthesized a set of shape- and size-controlled Pd nanoparticles and evaluated the effects of shape and size on reduction activity for nitrite, NDMA, and diatrizoate. In each case, the TOF_0 for nitrite, NDMA, and diatrizoate reduction is dependent on the geometry of surface Pd sites at low contaminant concentration, but the TOF_0 for nitrite reduction is very similar for all shape- and size-controlled Pd nanoparticles at high contaminant concentrations. A two-site model based on the Langmuir−Hinshelwood mechanism was developed to shed light on the change of structure sensitivity for nitrite reduction with contaminant concentration, and it suggests that both reaction and adsorption of H_2, nitrite, and NO play important roles. Both DFT simulations for the free energy change of adsorption and the mathematical model fit suggest that the competition between adsorbates shifts the structure sensitivity of nitrite reduction with changes in the contaminant concentration. Our study shows for the first time that the catalytic reduction activity for waterborne contaminant removal varies with the Pd shape and size, that catalysts can be tailored for better performance, and that Pd catalysts offer promise to treat simultaneously a variety of contaminants for drinking water.

■ ASSOCIATED CONTENT

Supporting Information

Details of synthesis and characterization of Pd nanoparticle catalysts; control experiments for nitrite reduction; analytical methods for reactants and products; relationships between total surface sites or specific sites and nanoparticle size; DFT simulations for free energy change of H_2, nitrite, and NO adsorption; TEM images of Pd nanoparticle catalysts before and after reduction; and solved parameter values for the Langmuir−Hinshelwood two-site model. This material is available free of charge via the Internet at http://pubs.acs.org.

■ AUTHOR INFORMATION

Corresponding Author

*Phone: 001-217-333-3822. E-mail: werth@illinois.edu.

Present Address

■Department of Civil and Environmental Engineering, the University of Iowa, Iowa City, Iowa 52242, United States

Notes

The authors declare no competing financial interest.

■ ACKNOWLEDGMENTS

This work was primarily supported by Water CAMPWS, a Science and Technology Center program of the National Science Foundation under Agreement No. CTS-0120978, and in part by King Abdullah University of Science and Technology. This work was performed in part at the Nano Research Facility (NRF), a member of the National Nanotechnology Infrastructure Network (NNIN), which is supported by the National Science Foundation under Grant No. ECS-0335765. TEM analysis was carried out in part at the Frederick Seitz Materials Research Laboratory Central Facilities (MRL), University of Illinois. We thank Professor Yujie Xiong at University of Science and Technology in China for training for shape- and size- controlled Pd nanoparticle synthesis when he was on the staff of the NRF at Washington University in St. Louis. We thank Dr. Danielle Gray of the School of Chemical Sciences 3M Materials Science Laboratory for performing XRD analyses. We thank Dr. Rick Haasch of MRL for performing XPS analyses. We thank Rudiger Laufhutte of the School of Chemical Sciences Microanalytical Laboratory for performing ICP-MS analyses. We thank Jian Li at the Department of Civil and Environmental Engineering for assisting in solving the two-site model. We thank Professor Michael Janik of Penn State University for consultation regarding computation of ion adsorption and for the use of his Statistical Thermodynamics spreadsheets.

■ REFERENCES

(1) Chaplin, B. P.; Reinhard, M.; Schneider, W. F.; Schüth, C.; Shapley, J. R.; Strathmann, T. J.; Werth, C. J. *Environ. Sci. Technol.* **2012**, *46*, 3655.

(2) Chaplin, B. P.; Roundy, E.; Guy, K. A.; Shapley, J. R.; Werth, C. J. *Environ. Sci. Technol.* **2006**, *40*, 3075.

(3) Prüsse, U.; Hähnlein, M.; Daum, J.; Vorlop, K. D. *Catal. Today* **2000**, *55*, 79.

(4) Chinthaginjala, J. K.; Lefferts, L. *Appl. Catal., B* **2010**, *101*, 144.

(5) Chen, H.; Xu, Z.; Wan, H.; Zheng, J.; Yin, D.; Zheng, S. *Appl. Catal., B* **2010**, *96*, 307.

(6) Shuai, D.; Chaplin, B. P.; Shapley, J. R.; Menendez, N. P.; McCalman, D. C.; Schneider, W. F.; Werth, C. J. *Environ. Sci. Technol.* **2010**, *44*, 1773.

(7) Hurley, K. D.; Shapley, J. R. *Environ. Sci. Technol.* **2007**, *41*, 2044.

(8) Davie, M. G.; Reinhard, M.; Shapley, J. R. *Environ. Sci. Technol.* **2006**, *40*, 7329.

(9) Lowry, G. V.; Reinhard, M. *Environ. Sci. Technol.* **2000**, *34*, 3217.

(10) Schreier, C. G.; Reinhard, M. *Chemosphere* **1995**, *31*, 3475.

(11) Yang, B.; Yu, G.; Huang, J. *Environ. Sci. Technol.* **2007**, *41*, 7503.

(12) Knitt, L. E.; Shapley, J. R.; Strathmann, T. J. *Environ. Sci. Technol.* **2008**, *42*, 577.

(13) Pintar, A.; Batista, J.; Levec, J.; Kajiuchi, T. *Appl. Catal., B* **1996**, *11*, 81.

(14) *Perchlorate: Overview of Issues, Status, and Remedial Options; PERCHLORATE-1*; Interstate Technology & Regulatory Council: Washington, D.C., 2005.

(15) Steger-Hartmann, T.; Länge, R.; Schweinfurth, H. *Ecotoxicol. Environ. Saf.* **1999**, *42*, 274.

(16) Doherty, R. E. *Environ. Forensics* **2000**, *1*, 69.

(17) Lecloux, A. J. *Catal. Today* **1999**, *53*, 23.

(18) van Ginkel, C. G.; Plugge, C. M.; Stroo, C. A. *Chemosphere* **1995**, *31*, 4057.

(19) Mitch, W. A.; Sedlak, D. L. *Environ. Sci. Technol.* **2002**, *36*, 588.

(20) Burow, K. R.; Nolan, B. T.; Rupert, M. G.; Dubrovsky, N. M. *Environ. Sci. Technol.* **2010**, *44*, 4988.

(21) Pankow, A.; Cherry, J. A. *Dense Chlorinated Solvents and Other DNAPLs in Groundwater*; Waterloo Press: Waterloo, Canada, 1996.

(22) Mitch, W. A.; Sharp, J. O.; Trussell, R. R.; Valentine, R. L.; Alvarez-Cohen, L.; Sedlak, D. L. *Environ. Eng. Sci.* **2003**, *20*, 389.

(23) Pehlivanoglu-Mantas, E.; Hawley, E. L.; Deeb, R. A.; Sedlak, D. L. *Water Res.* **2006**, *40*, 341.

(24) Bolyard, M.; Fair, P. S.; Hautman, D. P. *Environ. Sci. Technol.* **1992**, *26*, 1663.

(25) von Gunten, U.; Hoigne, J. *Environ. Sci. Technol.* **1994**, *28*, 1234.

(26) Comly, H. H. *J. Am. Med. Assoc.* **1987**, *257*, 2788.

(27) Weyer, P. J.; Cerhan, J. R.; Kross, B. C.; Hallberg, G. R.; Kantamneni, J.; Breuer, G.; Jones, M. P.; Zheng, W.; Lynch, C. F. *Epidemiology* **2001**, *12*, 327.

(28) *Toxocological Profile for N-Nitrosodimethylamine*; Agency for Toxic Substances & Disease Registry: Washington, D.C., 1989.

(29) *Integrated Risk Information System*; United States Environmental Protection Agency: Washington, D.C., 2005.

(30) Souliotis, V. L.; Henneman, J. R.; Reed, C. D.; Chhabra, S. K.; Diwan, B. A.; Anderson, L. M.; Kyrtopoulos, S. A. *Mutat. Res. Fundam. Mol. Mech. Mutagen.* **2002**, *500*, 75.

(31) *Perchlorate and Perchlorate Salts*; United States Environmental Protection Agency: Washington, D.C., 2005.

(32) Pomati, F.; Castiglioni, S.; Zuccato, E.; Fanelli, R.; Vigetti, D.; Rossetti, C.; Calamari, D. *Environ. Sci. Technol.* **2006**, *40*, 2442.
(33) Xie, L.; Shang, C. *Environ. Sci. Technol.* **2005**, *39*, 1092.
(34) Couri, D.; Abdel-Rahman, M. S.; Bull, R. J. *Environ. Health Perspect.* **1982**, *46*, 13.
(35) McIsaac, G. F.; David, M. B.; Gertner, G. Z.; Goolsby, D. A. *Nature* **2001**, *414*, 166.
(36) Jones, O. A. H.; Voulvoulis, N.; Lester, J. N. *Water Res.* **2002**, *36*, 5013.
(37) Lehman, S. G.; Badruzzaman, M.; Adham, S.; Roberts, D. J.; Clifford, D. A. *Water Res.* **2008**, *42*, 969.
(38) Davie, M. G.; Cheng, H.; Hopkins, G. D.; LeBron, C. A.; Reinhard, M. *Environ. Sci. Technol.* **2008**, *42*, 8908.
(39) Kapoor, A.; Viraraghavan, T. *J. Environ. Eng.−ASCE* **1997**, *123*, 371.
(40) Prüsse, U.; Vorlop, K. D. *J. Mol. Catal. A: Chem.* **2001**, *173*, 313.
(41) Chinthaginjala, J. K.; Bitter, J. H.; Lefferts, L. *Appl. Catal., A* **2010**, *383*, 24.
(42) Yoshinaga, Y.; Akita, T.; Mikami, I.; Okuhara, T. *J. Catal.* **2002**, *207*, 37.
(43) Zhang, F.; Miao, S.; Yang, Y.; Zhang, X.; Chen, J.; Guan, N. *J. Phys. Chem. C* **2008**, *112*, 7665.
(44) Xiong, Y.; Xia, Y. *Adv. Mater.* **2007**, *19*, 3385.
(45) Xia, Y.; Xiong, Y.; Lim, B.; Skrabalak, S. E. *Angew. Chem., Int. Ed.* **2009**, *48*, 60.
(46) Jia, C.-J.; Schuth, F. *Phys. Chem. Chem. Phys.* **2011**, *13*, 2457.
(47) Semagina, N.; Kiwi-Minsker, L. *Catal. Rev.: Sci. Eng.* **2009**, *51*, 147.
(48) Crespo-Quesada, M.; Yarulin, A.; Jin, M.; Xia, Y.; Kiwi-Minsker, L. *J. Am. Chem. Soc.* **2011**, *133*, 12787.
(49) Bratlie, K. M.; Lee, H.; Komvopoulos, K.; Yang, P.; Somorjai, G. A. *Nano Lett.* **2007**, *7*, 3097.
(50) Narayanan, R.; El-Sayed, M. A. *J. Phys. Chem. B* **2005**, *109*, 12663.
(51) Zhang, H. X.; Wang, H.; Re, Y. S.; Cai, W. B. *Chem. Commun.* **2012**, *48*, 8362.
(52) Issenberg, P. *Fed. Proc.* **1976**, *35*, 1322.
(53) Davie, M. G.; Shih, K.; Pacheco, F. A.; Leckie, J. O.; Reinhard, M. *Environ. Sci. Technol.* **2008**, *42*, 3040.
(54) Fleming, E. C.; Pennington, J. C.; Wachob, B. G.; Howe, R. A.; Hill, D. O. *J. Hazard. Mater.* **1996**, *51*, 151.
(55) Bollag, J.-M.; Myers, C. *Sci. Total Environ.* **1992**, *117−118*, 357.
(56) Kurama, H.; Poetzschke, J.; Haseneder, R. *Water Res.* **2002**, *36*, 2905.
(57) Ebbesen, S.; Mojet, B.; Lefferts, L. *J. Catal.* **2008**, *256*, 15.
(58) Zhang, R.; Shuai, D.; Guy, K. A.; Shapley, J. R.; Strathmann, T. J.; Werth, C. J. *ChemCatChem* **2012**, DOI: 10.1002/cctc.201200457.
(59) Xiong, Y.; Cai, H.; Benjamin, J.; Wang, J.; Kim, M. J.; Xia, Y. *J. Am. Chem. Soc.* **2007**, *129*, 3665.
(60) Xiong, Y.; Chen, J.; Wiley, B.; Xia, Y.; Aloni, S.; Yin, Y. *J. Am. Chem. Soc.* **2005**, *127*, 7332.
(61) Shao, M.; Yu, T.; Odell, J. H.; Jin, M.; Xia, Y. *Chem. Commun.* **2011**, *47*, 6566.
(62) Van Hardeveld, R.; Hartog, F. *Surf. Sci.* **1969**, *15*, 189.
(63) Le Bars, J.; Specht, U.; Bradley, J. S.; Blackmond, D. G. *Langmuir* **1999**, *15*, 7621.
(64) Li, Y.; Boone, E.; El-Sayed, M. A. *Langmuir* **2002**, *18*, 4921.
(65) Narayanan, R.; El-Sayed, M. A. *Nano Lett.* **2004**, *4*, 1343.
(66) Lundwall, M. J.; McClure, S. M.; Goodman, D. W. *J. Phys. Chem. C* **2010**, *114*, 7904.
(67) Silvestre-Albero, J.; Rupprechter, G.; Freund, H.-J. *J. Catal.* **2006**, *240*, 58.
(68) Owen, E. A.; Yates, E. L. *Philos. Mag.* **1933**, 472.
(69) Stokes, A. R.; Wilson, A. J. C. *Math. Proc. Cambridge* **1942**, *38*, 313.
(70) Perdew, J. P.; Chevary, J. A.; Vosko, S. H.; Jackson, K. A.; Pederson, M. R.; Singh, D. J.; Fiolhais, C. *Phys. Rev. B* **1992**, *46*, 6671.
(71) Blöchl, P. E. *Phys. Rev. B* **1994**, *50*, 17953.
(72) Kresse, G.; Furthmüller, J. *Phys. Rev. B* **1996**, *54*, 11169.
(73) Kresse, G.; Joubert, D. *Phys. Rev. B* **1999**, *59*, 1758.
(74) Nørskov, J. K.; Rossmeisl, J.; Logadottir, A.; Lindqvist, L.; Kitchin, J. R.; Bligaard, T.; Jónsson, H. *J. Phys. Chem. B* **2004**, *108*, 17886.
(75) Rostamikia, G.; Janik, M. J. *J. Electrochem. Soc.* **2009**, *156*, B86.
(76) Savizi, I. S. P.; Janik, M. J. *Electrochim. Acta* **2011**, *56*, 3996.
(77) Yeh, K.-Y.; Restaino, N. A.; Esopi, M. R.; Maranas, J. K.; Janik, M. J. *Catal. Today* **2012**, DOI: 10.1016/j.cattod.2012.03.011.
(78) Habas, S. E.; Lee, H.; Radmilovic, V.; Somorjai, G. A.; Yang, P. *Nat. Mater.* **2007**, *6*, 692.
(79) Piccolo, L.; Valcarcel, A.; Bausach, M.; Thomazeau, C.; Uzio, D.; Berhault, G. *Phys. Chem. Chem. Phys.* **2008**, *10*, 5504.
(80) Quintanilla, A.; Butselaar-Orthlieb, V. C. L.; Kwakernaak, C.; Sloof, W. G.; Kreutzer, M. T.; Kapteijn, F. *J. Catal.* **2010**, *271*, 104.
(81) Hirai, H.; Yakura, N. *Polym. Adv. Technol.* **2001**, *12*, 724.
(82) Crespo-Quesada, M.; Andanson, J.-M.; Yarulin, A.; Lim, B.; Xia, Y.; Kiwi-Minsker, L. *Langmuir* **2011**, *27*, 7909.
(83) Ranea, V. A.; Strathmann, T. J.; Shapley, J. R.; Werth, C. J.; Schneider, W. F. *ChemCatChem* **2011**, *3*, 898.
(84) Morin, C.; Simon, D.; Sautet, P. *Surf. Sci.* **2006**, *600*, 1339.
(85) Newton, M. A.; Belver-Coldeira, C.; Martinez-Arias, A.; Fernandez-Garcia, M. *Nat. Mater.* **2007**, *6*, 528.
(86) Bellare, A.; Dadyburjor, D. B.; Kelley, M. J. *J. Catal.* **1989**, *117*, 78.
(87) Sehested, J.; Gelten, J. A. P.; Helveg, S. *Appl. Catal., A* **2006**, *309*, 237.
(88) Carrasquillo, A.; Jeng, J.-J.; Barriga, R. J.; Temesghen, W. F.; Soriaga, M. P. *Inorg. Chim. Acta* **1997**, *255*, 249.
(89) Hammer, B. *J. Catal.* **2001**, *199*, 171.
(90) Novell-Leruth, G.; Valcárcel, A.; Pérez-Ramírez, J.; Ricart, J. M. *J. Phys. Chem. C* **2007**, *111*, 860.
(91) Watanabe, K.; Kokalj, A.; Inokuchi, Y.; Rzeznicka, I.; Ohshimo, K.; Nishi, N.; Matsushima, T. *Chem. Phys. Lett.* **2005**, *406*, 474.
(92) McCalman, D.; Kelley, K.; Werth, C.; Shapley, J.; Schneider, W. *Top. Catal.* **2012**, *55*, 300.
(93) Crozier, T. E.; Yamamoto, S. *J. Chem. Eng. Data* **1974**, *19*, 242.